In depth analysis of transfer length method application on passivated contacts under illumination

Léo Basset, Wilfried Favre, Olivier Bonino, Julien Sudre, Gilles Ménard, Jean-Pierre Vilcot

In depth analysis of Transfer Length Method application on passivated contacts under illumination

Léo Basset[a,b *], Wilfried Favre[a], Olivier Bonino[a], Julien Sudre[a], Gilles Ménard[a], Jean-Pierre Vilcot[b]

[a]Univ. Grenoble Alpes, CEA, LITEN, DTS, LPH, INES, F-38000 Grenoble, France

[b]Univ. Lille, CNRS, Centrale Lille, Univ. Polytechnique Hauts-de-France, UMR 8520 - IEMN - Institut d'Electronique de Microélectronique et de Nanotechnologie, F-59000 Lille, France

*Corresponding author. E-mail address: leo.basset@outlook.com

Abstract: Although solar cells operate under illumination, most electrical characterization methods are carried out in darkness, which implies some bias. In this work, we study the influence of light on the contact resistivity of the electron and hole contacts of a silicon heterojunction (SHJ) cell using the transfer length method (TLM) method in order to determine them in conditions representative of an operating solar cell at maximum power point. A specific fabrication process has been developed to preserve the passivation level. Therefore, we first focus on the patterning approach used for processing, and show that we can fabricate TLM samples with good passivation properties. Using simulations, we also discuss on the influence of inhomogeneities in the excess minority carrier spatial concentration on the TLM analysis. These inhomogeneities, due to shading, local damages in the passivation or to carrier drift under bias voltage make the measurement complicated to carry out without significant error. Our results suggest that the measurement is more precise in darkness and at very high injection levels, under rear illumination and a low voltage bias.

Keywords: heterojunction, passivated contacts, contact resistivity, TLM, operating conditions

1. Introduction

Silicon heterojunction (SHJ) solar cells have demonstrated potential to reach very high efficiency in recent years, notably holding the record for conversion efficiency on silicon device in IBC configuration [1], and efficiencies above 25% on full M2 wafer area both side contacted device [2–4].

However, there is still room for improvement, for instance by reducing parasitic absorption [5] or by improving the electric properties of the materials and interfaces. Notably, interface engineering could be an important lever to decrease resistive losses, as the electron and hole contacts have been identified as the main source of series resistance (R_s) [6–9]. Nonetheless, one important aspect neglected in most previous published approaches on series resistance evaluation is that solar cells operate under illumination; therefore, a characterization under dark conditions neglects the impact of the photogenerated carriers, which is susceptible to be significant on the electron and hole contact resistivity, $\rho_c(e^-)$ and $\rho_c(h^+)$, respectively.

Indeed, the electron and hole quasi-fermi levels as well as the local band bending close to the interfaces vary with illumination through the excess carrier density. Thus, this may impact some of the transport mechanisms involved at those interfaces, such as diffusion inside the a-Si:H layers, tunneling through spikes in the valence or conduction bands, etc. Therefore, the contact resistivity should rather be extracted under an excess minority carrier density that is representative of the operating conditions of a cell in Standard Test Conditions (STC) at Maximum Power Point (MPP). Consequently, we need to develop a methodology to study the impact of illumination on $\rho_c(e^-)$ and $\rho_c(h^+)$ values while guaranteeing maximum integrity with the real device properties (design, materials, thermal budget, passivation).

In this paper we first detail the prerequisites for precise contact characterization using the Transfer Length Method (TLM). Secondly, we present such a sample fabrication procedure that has been developed as to be the most representative of a real SHJ device, especially by preserving its passivation properties. Finally, we investigate the influence of illumination on the electron and hole contact resistivities using both experimental and simulation approaches.

2. TLM analysis for measurement of $\boldsymbol{\rho_c(e^-)}$ and $\boldsymbol{\rho_c(h^+)}$

To determine electron and hole contact resistivities of a SHJ cell, we use a methodology very close to that proposed by Lachenal et al. [6]. They proposed to apply the TLM [10] on some original structures where the ITO layer is etched between the electrodes, in order to avoid any lateral transport in ITO and so to force the current going through the whole contact stack, from the metal contacts to the c-Si. To study the electron contact n-type c-Si is used, and to measure the hole contact p-type wafers are necessary to avoid non-ohmic behavior. Note that the metal/ITO contact resistivity is comprised in the measurement of $\rho_c(e^-)$ and $\rho_c(h^+)$. However, it was evaluated to be negligible (<1m$\Omega.cm^2$) compared to the full stack, using dedicated TLM samples forcing current in the ITO and preventing current flow in bulk c-Si with an a-Si:H(p) layer at the front side (see e.g. [11]). Both contact resistivities are important for device operation and modeling [12], but on this work, we focus only on the electron and hole contacts.

In order to observe the effect of photogenerated carriers we need the samples to be passivated. Our samples only differ from those in [6] by the rear side, that is here passivated and by the silver electrodes, that are screen-printed instead of sputtered in [6] for a better similarity to a real SHJ cell process (see Figure 1).

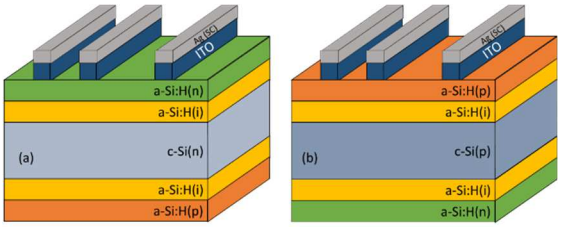

Figure 1: (a) n and (b) p-type stack TLM samples for extraction of the electron and hole contact parameters, respectively (texturing is not illustrated)

2.1 TLM analysis

The TLM allows determining the sheet resistance of a layer (R_{Sh}), and the contact resistance (R_C) between this layer and a metallic electrode. It relies on the measurement of the I-V characteristic in between electrodes of length L and width W, with various spacing (d) (see Figure 2).

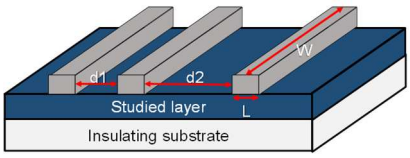

Figure 2 : Schematic of a typical structure for TLM analysis

For ohmic contacts, the resistance R_{TLM} reads:

$$R_{TLM}(d) = 2R_C + \frac{R_{Sh}}{W} * d \qquad \text{Eq. 1}$$

Therefore, using the TLM curve, $R_{TLM} = f(d)$, R_C is easily extracted from the y-axis intercept and R_{Sh} from the slope ($R_{Sh} = slope * W$). To determine the contact resistivity (ρ_C), metric independent of the electrode geometry, the TLM model invokes the concept of transfer length (L_t), distance over which the majority of the current crosses the contact, and reads:

$$R_C = R_{Sh} * \frac{L_t}{W} * \coth\left(\frac{L}{L_t}\right) \qquad \text{Eq. 2}$$

L_t is then determined by solving Eq. 2, and ρ_C reads:

$$\rho_C = R_{Sh} L_t^2 \qquad \text{Eq. 3}$$

The TLM formulas presented before are only valid by approximating that the samples are perfectly homogeneous across their width, so that the 3D structure in Figure 2 can be simplified to a 2D one. A top view of a TLM sample is represented in Figure 3.

The distance separating the edges of a TLM electrode and that of the sample, δ, should be kept minimal. If this is not the case, 3D current flow (i.e non-straight current lines) takes place at electrode extremities, when a voltage is applied (see Figure 3). Using long electrodes so that $w \to W$ also minimizes this parasitic effect on the data extraction [13].

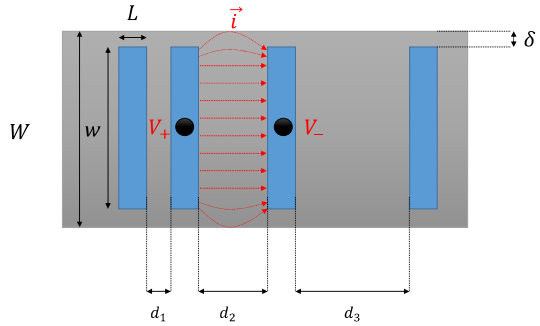

Figure 3 : Top view of a TLM structure. Current lines are represented in red

A simple way to get rid of these "edge currents", whatever w is, is to cut the sample up to the electrode edge, to simply get $W = w$. As an example, we present on Figure 4 results obtained from two n-stack TLM samples (see Figure 1(a)) with different electrode width (10 and 20mm) before and after cutting the edges (δ = 3-6mm). Contact probes are positioned approximately at the center of the electrode. R_{Sh} value is compared with that determined using the 4 point-probe technique (4PP) on sample surface.

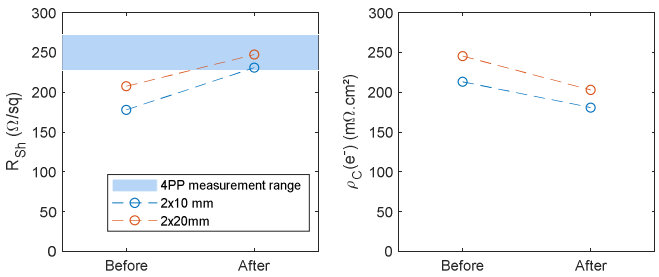

Figure 4: Sheet resistance (a) and contact resistivity of the electron contact (b) determined for 10mm and 20mm wide TLM electrodes before and after outer edges cut (electrode length is 2mm)

Before cutting the edges, we observe that TLM leads to R_{Sh} values below that determined with the 4PP technique. After cutting the edges, the R_{Sh} values from TLM analysis are within the uncertainty range of the 4PP determination. Oppositely, ρ_C decreases after edge cutting. Therefore, the δ space leads to errors in the parameter determination from TLM measurement, with an underestimated R_{Sh} and an overestimated ρ_C. In the following we systematically cut the edges along the outer edge of the electrodes.

Another factor which is susceptible to have an important impact on the TLM results is the conductivity of the electrodes. The TLM model assumes equipotential electrodes all along w. This is rarely encountered in the practical case since measurement probes are usually not covering all electrode width and electrodes are not perfectly conductive. Therefore, a voltage drop occurs along the electrode width, which would also lead to a 3D current flow. Often in the literature, metallic TLM electrodes are deposited using PVD or evaporation, e.g. [6,9,14]. These electrodes are then very thin, a few hundred nanometers maximum, and therefore are poorly conducting - even though the metal conductivities are very high -, leading to such potential drops along the electrode width and bias in the TLM results. In former experiments using evaporated electrodes, non-reproducibility in I-V characteristics were observed. Slight modifications in the probe position on the electrode would modify the I-V curve, and this would result in very noisy TLM curves. This effect becomes much smaller with screen-printed electrodes. Another occurrence of this potential drop issue occurs when too narrow electrodes are used, for example when using finished cut strips of cells [15]. To make sure that this effect stays minimal, the electrodes should be as conductive as possible. In this work, all electrodes are screen-printed (i.e. conductivities of the order of $5\mu\Omega.cm$ and thicknesses of the order of 10µm), moreover using the same fabrication process than the real cell.

We fabricated TLM samples (p-type stack) using substrates of $1.16\Omega.cm$ resistivity and of 155µm thickness, with varying electrode width and length. The sheet resistance value, R_{Sh}, is extracted with a good reproducibility whatever the electrode geometry is (Figure 5 (a)). A variation may appear for too large widths as most samples exhibit a decrease of R_{Sh} for $W = 30mm$, but it is not very significant. This indicates that our choice for screen-printed electrodes is appropriate, as they are sufficiently conductive for voltage drops to be negligible.

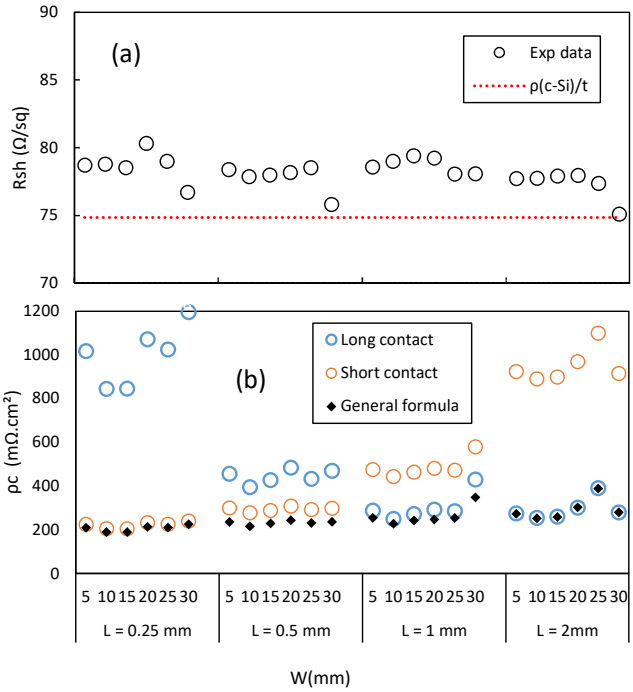

Figure 5: (a) R_{Sh} and (b) ρ_C extracted using TLM as a function of electrode geometry. ρ_C is extracted using either the general formula (Eq. 2) or long (Eq. 4) or short (Eq. 5) contact approximations. (4 different lengths, 0.25, 0.5, 1 and 2 mm, and 6 different widths from 5 to 30 mm by 5 mm step).

Additionally, a useful simplification of the TLM model relies on the 'long contact approximation'. If the transfer length is very small compared to L, then Eq. 2 becomes:

$$R_C = R_{Sh} * \frac{L_t}{W} = \frac{\rho_C}{L_t W} \quad \text{Eq. 4}$$

Oppositely, the 'short contact approximation' reads:

$$R_C = R_{Sh} * \frac{{L_t}^2}{LW} = \frac{\rho_C}{LW} \quad \text{Eq. 5}$$

Both these expressions are easier to solve than Eq. 2, which requires iterative calculation, and apply in boundary cases. However, the long contact expression is frequently assumed without verifying if it applies (e.g. [6]). Using the previous sample set, we extract the contact resistivity of the hole contact according to the full formula or the long or short contact approximations (Figure 5 (b)).

With the general formula, we observe no significant effect of the electrode geometry, and W has little importance. However, we observe that with both approximation formulas, depending on L the value of $\rho_C(h^+)$ determined can be 3 times higher than the value obtained from the general formula. In this work, we exclusively use the general formula. L_t is determined in between 0.5 and 0.7 mm for all samples, which is near the tipping point where the "long contact" and "short contact" approximations become more accurate than the other.

The TLM model also assumes that the sample is very thin, so that the hypothesis that current is homogeneous in the layer can be considered. When studying thin films, this assumption is not a problem, but some issues arise when studying a thick c-Si base. Typically the thickness of the sample must be small compared to the electrode length (L) and to the inter-electrode spacing (d) [16] in order to minimize the effect of the current density inhomogeneity. In the following we use samples with thickness $t = 160\mu m$, electrode length of $L = 500\mu m$, and restricted the inter-electrode distances to $d > 300\mu m$. We made sure that we are unaffected by the dimensions of our samples with simulation (see Supplementary Material). Also, Eidelloth and Brendel proposed an extended TLM model, to correct for 2D effects when using thick substrates ([16]). We implemented it and found that for all the experimental values presented in this work it led to a relative difference in ρ_C below 0.6% as compared to standard TLM, so we did not consider it in the following.

3. Fabrication processes and passivation control

In the following, we detail the TLM sample fabrication procedure that has been used for the sample structure to be as identical as possible to that of real cell focusing particularly on ITO delimitation process including passivation quality check.

3.1 Fabrication process flow

In order to fabricate samples such as presented in Figure 1, we first fabricated solar cell precursors (see [17]), and then we patterned the ITO and deposited the electrodes.

The patterning of the ITO is realized using a hot-melt resist masking approach and subsequent wet etching of the ITO and removal of the hot-melt patterns. The organic hot-melt is deposited in order to design the TLM electrodes using an inkjet printer from Ceraprint, and hot-melt waxes provided by SunChemical. Temperature is kept below 150°C so we expect no damages to the a-Si:H layers due to thermal degradation. ITO is etched using a highly concentrated HCl solution [18] and the hot-melt is subsequently removed. Then, we align the screen-print mesh to deposit silver electrodes on top of the ITO patterns, and the samples are cured at approximately 200°C for up to 30 minutes, similarly to the standard SHJ cell fabrication procedure. Finally, samples are cut along the outer edges.

With this fabrication procedure, we expect to have test vehicle well representative of a typical SHJ device (layers, passivation properties, interfaces, thermal budget, etc.), In the next parts, we study the relevance of this process flow focusing on ITO removal and passivation properties.

3.2 Selective ITO etching

To qualify the ITO removal process, we prepared polished M2 (156.75mm x 156.75mm) Cz n-type c-Si wafers by wet polishing, and deposited the a-Si:H/ITO stacks at both surfaces (see Figure 1 (a)). The samples were then immersed in concentrated HCl up to 360s, some wafers being picked every 60s from the solution rinsed in deionized water and dried. We monitored the ITO etching status using spectroscopic ellipsometry technique for the various durations, as presented on Figure 6. A sample without ITO deposition served as a reference. We observed that as the etch time in HCl increases, the imaginary part of the dielectric constant (ε_i) signal changes drastically, especially after 180s where the characteristic peak of the ITO around 3.5-4 eV disappears completely. After 360s, ε_i matches with the one obtained for the reference sample, indicating a complete removal of the ITO without affecting a-Si:H layers thicknesses.

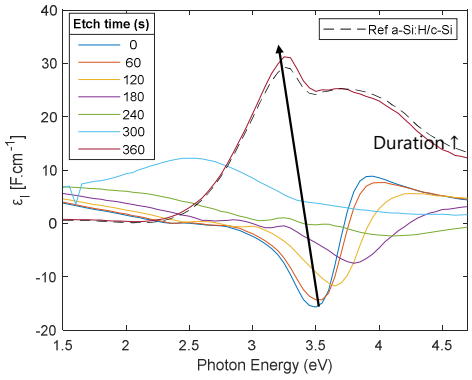

Figure 6: Imaginary part of the dielectric constant measured with ellipsometry for samples that were immersed in HCl for times between 0 and 360s. The arrow is a guide to the eye. A reference sample with a-Si:H on c-Si (no ITO) is also presented for comparison.

3.3 Selective hot-melt removal

For the hot-melt removal, a KOH solution was indicated by the hot-melt provider. Indeed, we found the hot-melt can be removed efficiently, but KOH solution being known to etch a-Si:H layers [19], the passivation was degraded to a very low level (see Figure 7 (a)) even using a 1wt% KOH solution during 1 minute. The a-Si:H(p) layer was however found to resist KOH with no degradation (not shown). Nevertheless, we developed a KOH-free approach that demonstrated a fast hot-melt removal that much less harms the passivation level (Figure 7 (b)). After hot-melt removal, we did observe a slight lifetime degradation, but for all samples we got $iV_{OC} \geq 730mV$ and $iFF \geq 84.5\%$, even after an overly long hot-melt stripping (5 times the necessary duration), which gives a convenient process safety margin.

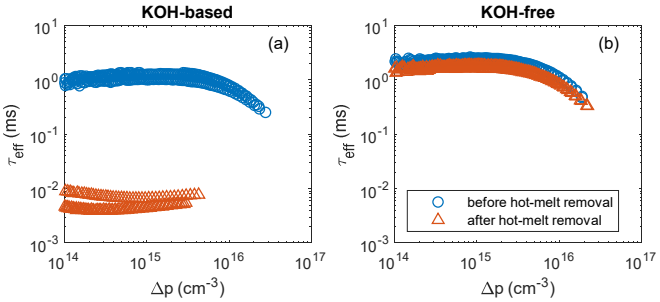

Figure 7: Effective lifetime as a function of minority carrier density measured on cell precursors (two to three samples for each condition) before and after hot-melt removal step: (a) 1 min in the KOH-based solution and (b) 5 min in the KOH-free solution

Finally, samples are metallized and cut along the edges of the electrodes. These steps can also cause some damages to the passivation. At this stage, passivation level could not be properly assessed on metallized samples but a good passivation uniformity was confirmed using uncalibrated photoluminescence (PL) imaging mode from a LIS-R2 tool from BT Imaging (Figure 8).

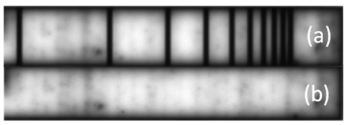

Figure 8: PL image of samples (a) from metallization side, and (b) from non-metallized side (the image was reversed to correspond to (a))

3.4 On the use of patterning methods

The use of patterning instead of simpler methods could be questioned: in the literature, some groups fabricated similar samples using shadow mask approaches (e.g. [14]). In this case the ITO is sputtered through a hard mask to form the patterns. This is much easier to implement as the patterning approach involves some masking and etching steps.

We confronted the two approaches for the fabrication of our TLM samples, and compared the edges of the samples. The patterning technique is described above and for the masking approach, we used a metallic mask patched on top of a sample for the ITO PVD deposition step. First, under visual inspection (Figure 9 (a)), we observe that the edges of the sample using the masking technique have a blur brownish zone across the edges, which is not observed on the sample fabricated using the patterning method. This suggests that some deposition takes place under the edge of the mask. This is confirmed with SEM imaging (Figure 9 (b)): the thickness of the ITO layer in a direction perpendicular to its edge was measured on both patterned and masked samples. Very sharp delimitation between patterned and un-patterned zones of approximately 10µm is obtained with the patterning approach, while it extends over one millimeter for the masking approach (Figure 9 (c)). This confirms the a-Si:H/ITO/Ag interface to be better delimitated when using the patterning approach.

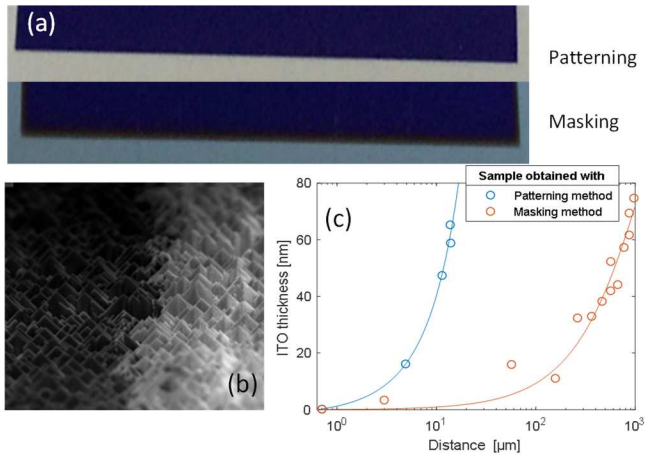

Figure 9: (a) Pictures of ITO surface areas obtained with the patterning (top) and masking (bottom) techniques. Both widths are approximately 2cm. (b) SEM image at the vicinity of the edge of the ITO pattern (with the patterning method) (c) profiles of ITO thickness perpendicular to the pattern edge with both methods

4. TLM measurements under illumination

4.1 Validation of the measurement in the dark

We demonstrated that the developed patterning process of ITO upholds the initial very good passivation level of the samples and allows achieving structures as shown in Figure 1. First, n and p-stack TLM samples are fabricated using approximately 160µm thick wafers of respective resistivity value, $\rho_{n-type} = 2.27\ \Omega.cm$ and $\rho_{p-type} = 1.12\ \Omega.cm$. The effective lifetime for the samples was monitored at the end of the ITO deposition process and before the patterning steps. It was measured as $\tau_{eff}(\Delta n = 10^{15} cm^{-3})$=2.3ms for the n-type samples, and 84µs for the p-type sample (attributed to the low τ_{bulk} of the production grade p-type wafers used). We start by proof-testing our approach for sample fabrication with measurements in the dark (Figure 10).

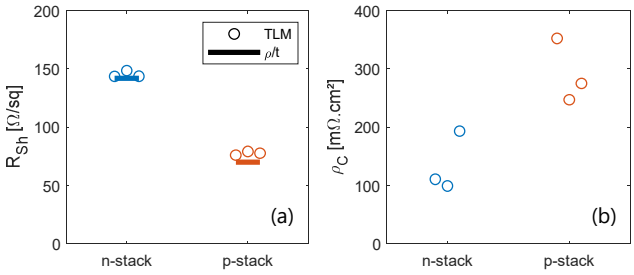

Figure 10: Measured values of (a) sheet resistance and (b) contact resistivity for n and p-stack TLM samples. The expected R_{Sh} from thickness and resistivity data of the samples are also displayed in (a)

The measured sheet resistance allows calculating the resistivity of each sample from the relation $\rho = R_{Sh} * t$: we found $\rho_{n-type} = 2.25\ \Omega.cm$ and $\rho_{p-type} = 1.21\ \Omega.cm$, which is in close agreement with the expected values. The average values of measured contact resistivity are also in good agreement with that reported by other authors, $\rho_c(e^-) = 133.8\ m\Omega.cm^2$ ($140\ m\Omega.cm^2$ in [6]) and $\rho_c(h^+) = 291.1\ m\Omega.cm^2$ ($240\ m\Omega.cm^2$ in [6]), with a hole contact resistivity higher than its electron counterpart. Theoretical variation of the resistivity under illumination

To further confirm the validity of our TLM measurement procedure under illumination, we propose to monitor variations of the bulk resistivity obtained from the R_{Sh} extraction for different steady-state illumination intensities, and to compare it with values obtained from modelling.

The bulk resistivity is highly dependent on the minority carrier density under illumination. It can be expressed in the case of no trapping ($\Delta n = \Delta p$), as:

$$\frac{1}{\rho} \sim q * \left(\mu_n * (N_D + \Delta p) + \mu_p \Delta p\right) \qquad \text{Eq. 6}$$

Where μ_n and μ_p are the electron and hole mobilities in the c-Si wafer. In this work they are calculated according to [20,21].

To infer the effect of steady-state illumination, one has to consider both generation and recombination rates. The average generation rate (G_{av}) and average excess minority carrier density (Δp_{av}) are linked through:

$$\tau_{eff} = \frac{\Delta p_{av}}{G_{av}} \qquad \text{Eq. 7}$$

With:

$$G_{av} = \frac{E * f_{abs} * N_{ph}^{1sun}}{t} \quad \text{Eq. 8}$$

Where E is the illumination level, f_{abs} is the fraction of absorbed incidents photons, N_{ph}^{1sun} is the photon flux under 1 Sun illumination, and t is the wafer thickness.

τ_{eff} can be expressed as:

$$\frac{1}{\tau_{eff}(\Delta p)} = \frac{1}{\tau_{S,front}(\Delta p)} + \frac{1}{\tau_{S,rear}(\Delta p)} + \frac{1}{\tau_{SRH}(\Delta p)} + \frac{1}{\tau_{int}(\Delta p)} \quad \text{Eq. 9}$$

Where τ_{int} is the intrinsic lifetime, τ_{SRH} is the SRH-limited lifetime, and $\tau_{S,front}$ and $\tau_{S,rear}$ are the front and rear surface recombination-limited lifetimes. In our approach, we consider SRH recombination using [22], intrinsic recombination according to Richter's model for p-type samples [23], and Veith-Wolf reassessment for n-type samples [24]. Surface recombination is calculated using the approach from Garin et al. [25].

From Eq. 6, Eq. 7, Eq. 8 and Eq. 9 we can determine $\rho = f(E)$. We consider that shading from the metallic electrodes affects the cell homogeneously so that f_{abs} is reduced by a factor (1-sh), where sh is the fraction of the sample area covered by the electrodes.

4.2 Validation of the approach under illumination

TLM measurements were conducted for both n and p-stack samples as a function of the illumination intensity (top illumination). I-V curves are displayed in Figure 11 for the n-stack TLM sample.

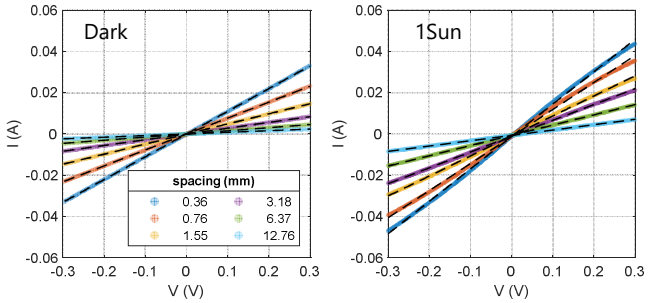

Figure 11: I-V curves for an n-stack sample for each spacing at ambient temperature; (left) under dark conditions and (right) under 1 Sun illumination. Experimental data is plotted as transparent colored lines and linear fits are plotted as black dashed lines.

The measured I-V curves stay quite linear under illumination, even though we observe a slight rectifying behavior (the p-stack sample is not shown but features better linearity). To ensure a good linearity, we restrict the TLM analysis to the -0.1V to 0.1V range for all samples in this work. This is also motivated by the drift of carriers that is negligible only at small bias [26], which we will discuss in the following.

The TLM plots are also no longer purely linear under illumination, and R^2 diminishes with increasing light intensity. However, we get R^2>0.995 for all the illumination intensities tested so we consider the precision satisfying. Finally, we apply the TLM analysis (Figure 12).

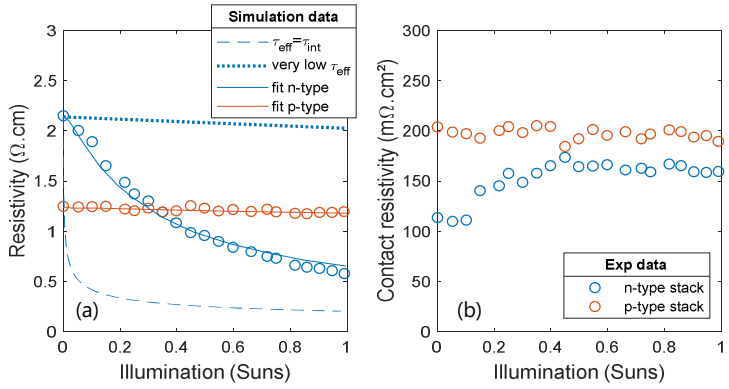

Figure 12: (a) c-Si resistivity and (b) electron/hole contact resistivities as a function of illumination intensity. Dots are experimental data and lines are simulation results. The simulation condition with very low τ_{eff} considers $\tau_{eff}(\Delta p = 10^{15} cm^{-3}) = 7.4 \mu s$

For the p-stack sample, no significant effect of light is pointed out. However, for the n-stack sample the determined resistivity decreases when illumination intensity increases, and the determined ρ_c value increases from 114 $m\Omega.cm$ in the dark to 160 $m\Omega.cm$ under 1 Sun illumination. This demonstrates that indeed the excess minority carrier density has an impact on the characterization of ρ_c. This also emphasizes that high lifetime values are needed to observe an effect of light on ρ_c, through the excess minority carrier density.

We applied the resistivity modelling approach with different sets of parameters (lines in Figure 12) and compared it to experimental data. First, for the n-type sample, we considered two extreme cases without shadowing. We found that if the effective lifetime equals the intrinsic lifetime (dashed

curve on Figure 12(a)), then a very drastic drop of c-Si resistivity is expected even at low illumination levels. Oppositely, for low τ_{eff} value (dotted curve on Figure 12(a)) we expect a low variation of the resistivity at illumination up to 1 Sun. We parameterized our effective lifetime model from PCD measurements after the patterning steps, and considered a high shadowing value of $sh = 72\%$ to fit our data (higher than the geometrical shadowing of the samples ~25%). We reach a good agreement with both n and p-type data (see solid lines in Figure 12 (a)). The absence of clear effect of illumination on the p-type sample resistivity (and possibly contact resistance) is thus attributed to the small increase of the excess carrier density (with respect to initial doping concentration) with increasing illumination intensity. Damages in the passivation from cutting and handling introduces some error in the lifetime parameterization, but the fact that our modelling can fit data gives credence to the corresponding measurements of contact resistivity.

Note that the samples were measured in conditions representative of open-circuit, as the junction is not polarized. Therefore, the excess minority carrier under 1 Sun illumination is higher than it would be in a cell operating in STC conditions at MPP. Hypothesizing a realistic value of $\Delta p_{MPP} = 1e15\ cm^{-3}$, this corresponds to an illumination intensity of about 0.25 Suns, and to a contact resistivity of 157 $m\Omega.cm^2$.

4.3 TCAD simulation of TLM samples

We perform TCAD measurements using Silvaco Atlas in order to simulate n-stack TLM samples (Figure 13).

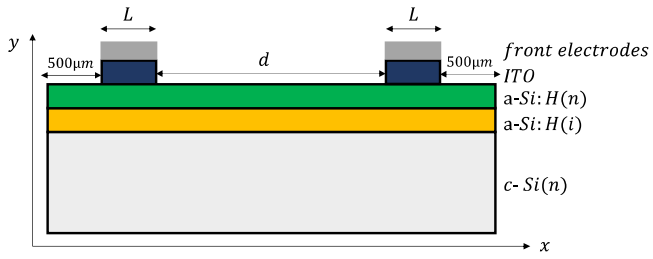

Figure 13: Simulated TLM test structure

The interelectrode spacing d is in the range 300-850 µm, and $L = 500\mu m$ to correspond to our experimental samples. An I-V sweep is then performed for each spacing and ρ_C and ρ are extracted following the TLM analysis described above. Assumptions in the TLM analytical theory can lead to artifacts in the determination of ρ_C (see e.g. [27]), which are thus present in both experimental and in the 2D TLM modeling results, allowing for 1:1 comparison.

The main parameters are displayed in Table 1.

Table 1: Main parameters used for the TLM modelling with TCAD software

Quantity	**c-Si**	**a-Si:H(n)**	**a-Si:H(i)**	**ITO**
Band gap (eV)	1.12	1.75	1.65	3.65
Relative permittivity	11.9	11.9	11.9	20
Electron affinity (eV)	4.05	3.9	3.9	4.45
Thickness	160µm	3.5 nm	3.5 nm	70 nm
Doping / Activation energy	$1.72 * 10^{15} cm^{-3}$	0.2eV	0.55eV	$1.25 * 10^{20}\ cm^{-3}$

The left, right and bottom edges are left bare so that there is no recombination at these points. The metal/ITO contact is considered perfectly ohmic with zero contact resistance. We calibrated the lifetime of the sample introducing a single mid-gap defect in the c-Si with $\tau_{p0} = 10\ \tau_{n0} = 5.785 * 10^{-3} s$. To model surface defects at the c-Si/a-Si:H interface, a highly defective 1nm thick c-Si layer was introduced, equivalent to a D_{it} of $10^9 cm^{-2}$ [28]. a-Si:H layers are modelled considering tail states and defect states using the Defect-Pool model, with realistic model parameters values [29], and the doping of the layers were adapted to fit experimental values of activation energies [30]. Optical parameters for the a-Si:H and ITO layers are based on characterization of the optical refractive index of experimental layers. Reduced reflections are considered at the front surface due to the textured surface.

Silvaco Atlas features many different carrier transport models that can be enabled. In our simulation, we use Yang's model for thermionic emission over heterojunctions at the a-Si:H/ITO and c-Si/a-Si:H interfaces [31]. All other transport mechanisms are the automatically implemented models. The electron affinity of the ITO was set to 4.45eV in order to fit experimental values of $\rho_C(e^-)$ in the dark for the sample presented in Figure 15.

4.4 Influence of front or rear illumination

We have discussed that the contact resistivity is related to the excess minority carrier density. However, with an inhomogeneous excess carrier density across the sample, the TLM model is not valid anymore, as it assumes a layer and a contact of homogeneous properties. These inhomogeneities can be caused by different effects, such as electrode shading, or local passivation inhomogeneities. A more thorough approach for TLM measurements could be to measure samples under rear side illumination. This removes shading due to the electrodes and should lead to a more homogeneous photogeneration rate (G_{ph}) over the sample.

G_{ph} varies across the thickness of the sample, due to the Beer-Lambert law. Additionally, it changes with reflection/transmission properties of the sample leading to spatial inhomogeneity across the sample width. In the case of steady-state illumination with an inhomogeneous G_{ph} value across an n-type sample, the continuity equation reads for an n-type material [32]:

$$\frac{\Delta p(x,y)}{\tau_{eff}(x,y)} = G_{ph}(x,y) + D_p\left(\frac{\partial^2 \Delta p_x}{\partial x^2} + \frac{\partial^2 \Delta p_y}{\partial y^2}\right) \qquad \text{Eq. 10}$$

Where D_p is the diffusion coefficient of holes.

Therefore, with an inhomogeneous G_{ph} value we expect variations of Δp across the sample, which can be attenuated by the hole diffusion over sufficiently short distances.

We simulated n-stack TLM samples on Silvaco Atlas, considering either front illumination, rear illumination or front illumination with perfectly transparent Ag/ITO contact stacks (i.e. $sh = 0$). First, we studied the spatial evolution of the photogeneration rate (G_{ph}) and excess minority carrier density (Δp) (Figure 14).

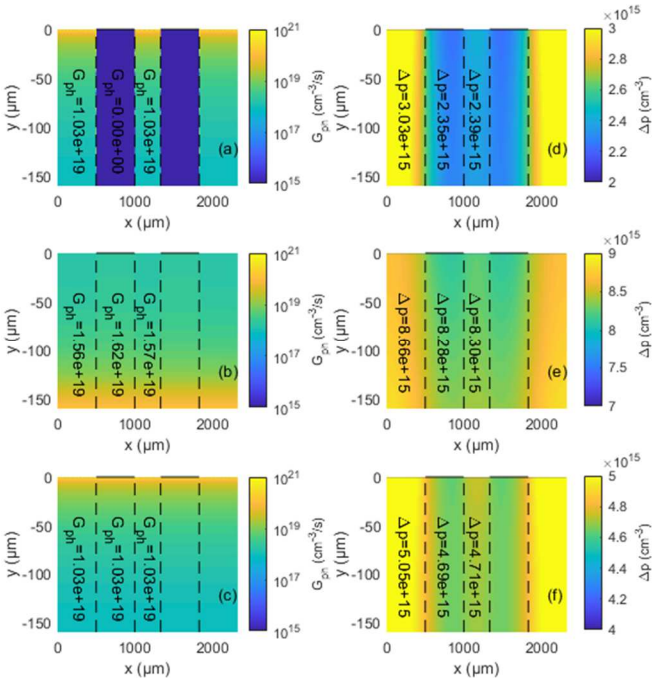

Figure 14: Simulated cross-section of TLM samples representing (a)-(c) photogeneration rate (G_{ph}) and (d)-(f) Δp at V_{OC} under 1 Sun illumination for (a) and (d) front illumination, (b) and (e) rear illumination and (c) and (f) front illumination with perfectly transparent ITO/Ag contact stack. Values in black represent the integral of Δp or G_{ph} in the c-Si within the dotted region.

We found that with 1 Sun front illumination (Figure 14 (a)) there is no photogeneration below the metallic electrodes, which leads to inhomogeneities of Δp along the x-axis (Figure 14 (d)): it differs below and in between electrodes and at the sample edges. Along the y-axis, inhomogeneities are smaller as the sample thickness is sufficiently low such that diffusion practically homogenizes Δp. At the edges of the samples, carriers can only diffuse inwards. Diffusion does not compensate the inhomogeneities in G_{ph} along the x-axis.

With rear illumination (Figure 14 (b)), G_{ph} is more homogeneous along x, but still not completely, notably due to internal reflection below the electrodes which leads to locally higher G_{ph}. As there is no shading nor parasitic absorption in a-Si:H layers, the integrated G_{ph} over the sample is larger, leading to overall larger Δp. Homogeneities in Δp (Figure 14 (e)) are also reduced as compared to front illumination, but do not completely disappear.

Finally, with front illumination, but with perfectly transparent Ag/ITO electrodes (Figure 14 (c)), G_{ph} is homogeneous all across the length of the sample, but we still do not get completely homogeneous Δp (Figure 14 (f)), indicating that τ_{eff} is also inhomogeneous. In fact, the recombination rate in the c-Si right below a-Si:H layers in contact with ITO is different than below a-Si:H layers in contact with air in our simulation, and we do

expect similar result for real TLM structures. In the following, we exclude the latter case as it cannot be obtained experimentally, and does not lead to completely homogeneous Δp anyway.

We fabricated a new batch of n-type samples, trying to minimize defectivity as much as possible, and compared front and rear illumination experimental results, and confronted the results with simulation (Figure 15). Note that for experimental data with rear illumination we used a back-illumination source and a transparent chuck that cannot enable temperature control, whereas a temperature regulated chuck was used for front illumination condition.

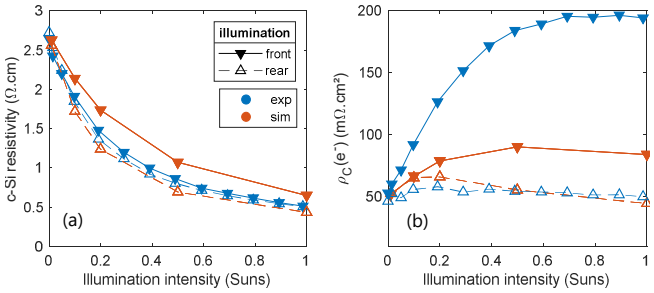

Figure 15: experimental (blue) and simulated (orange) values for c-Si resistivity and $\rho_C(e^-)$ as a function of front and rear illumination intensity.

In Figure 15 (a), we observe that simulated c-Si resistivity values are lower at a given illumination with rear illumination than with front illumination. The effect is similar experimentally even though trends are not as marked due to measurement error and thermal fluctuation in the rear illumination mode.

In terms of contact resistivity, considering both experimental and TCAD data, we observe larger variations of $\rho_C(e^-)$ with illumination intensity under front illumination as compared to rear illumination (Figure 15 (b)). This indicates that part of the variation of $\rho_C(e^-)$ with illumination in the front illumination case is an artifact of the measurement, due to inhomogeneous Δp across the sample. With rear illumination, the measurement artifacts are weaker, but as we demonstrated that Δp is still not completely homogeneous in this case, the observed variation may still be an artifact.

4.5 Influence of measurement conditions

To investigate these results more deeply, we conducted some additional simulations in the rear illumination mode. First, we studied the influence of illumination intensity on Δp inhomogeneity (Figure 16). We found that at low illumination intensity, Δp inhomogeneities are more pronounced: at 0.01 Sun, the relative difference in Δp values between and below the electrodes is approximately 23%, while under 1 Sun the difference is only about 0.2%. This shows that we expect a larger bias in the measurements at low illumination intensities.

In addition, carrier drift when biasing the electrodes can also lead to an erroneous TLM analysis. We simulated with TCAD the spatial inhomogeneities of Δp under different biases (Figure 17). We found that as the bias voltage increases, Δp inhomogeneities are exacerbated, and this results in non-linear I-V curves [26]. At 100mV, the integrated Δp value below the left electrode is 83% higher than under the right electrode, while at 1mV the relative difference is only 1%. When no voltage is applied Δp is of course equal below the two electrodes (Figure 14 (e)). Restricting the range of voltages used therefore reduces Δp inhomogeneities and should reduce non-linearities and lead to less error in the TLM analysis. Using only data in the range (-1mV;1mV) slightly changes the $\rho_C(e^-)$ determined as compared to the displayed values in Figure 15 (less than 6% relative difference for all points of the curve). This indicates that the Δp inhomogeneities only have a small impact on the linearity of the I-V curves in this voltage range, which was also seen experimentally (Figure 11).

Finally, inhomogeneous τ_{eff} due to local degradations of the surface passivation may cause additional measurement artifacts due to Δp inhomogeneities. A rigorous determination would therefore require very good G_{ph} and τ_{eff} homogeneity all across the sample which is experimentally unpractical due to defectivity [33,34] and edge cutting deterioration.

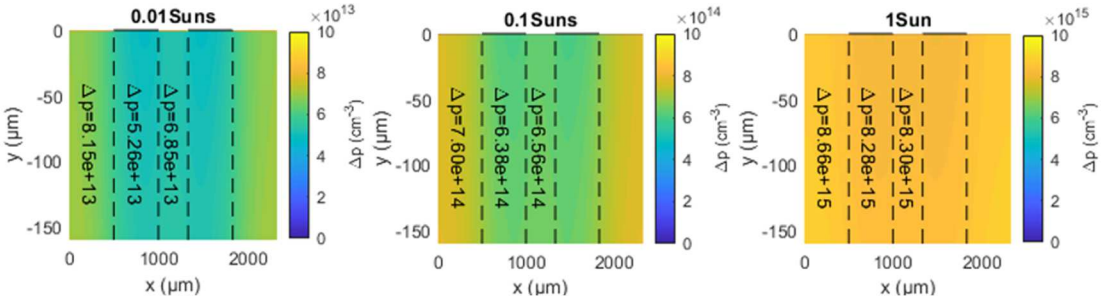

Figure 16: Simulated cross-section of TLM samples representing Δp with $N_D = 1.72 * 10^{15} cm^{-3}$ at V_{OC} for 0.01, 0.1 and 1 Sun illumination intensities respectively.

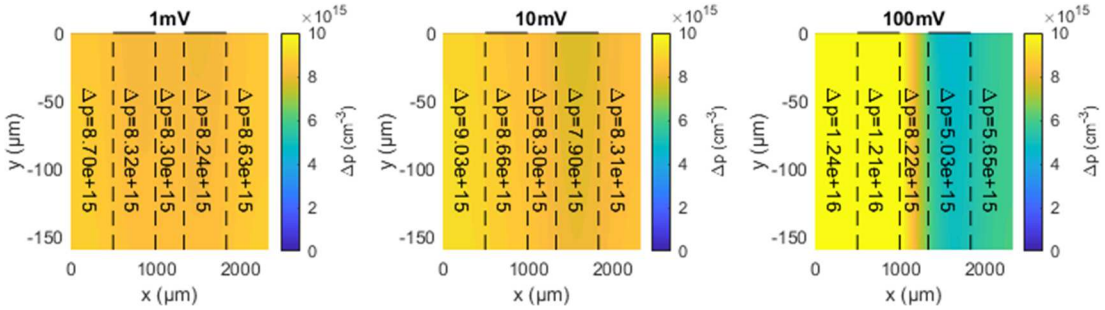

Figure 17: Simulated cross-section of TLM samples representing Δp under 1 Sun rear illumination and +1, +10 and +100 mV bias voltages (Voltage is applied at the right electrode).

Similarly than with front illumination, the inhomogeneities stemming from these effects may be the cause of artefactual variations of $\rho_C(e^-)$ under illumination.

4.6 Influence of wafer doping

Studying the case of samples with different wafer doping levels, i.e. c-Si resistivity values, is interesting as it allows comparing the effect of fixed charges and photogenerated charges. Indeed, lowly doped samples tend to function at higher injection levels ($\Delta p/N_D$) than highly doped samples. Also, band bending close to the interface is linked to the c-Si doping level, so that we expect a similar effect of illumination and doping on $\rho_C(e^-)$.

We investigate three c-Si doping densities: $6.89 * 10^{14} cm^{-3}$, $1.72 * 10^{15} cm^{-3}$ and $1.08 * 10^{16} cm^{-3}$, with rear illumination, both by simulation and by experimental characterization. We investigate illumination intensities up to 1 Sun experimentally, and up to 10 Suns in the simulations. Except for the c-Si doping, all the other parameters for the simulation are kept constant (see Table 1). We can calculate Δp at a given illumination using ρ measured at this illumination level and in the dark (ρ_{dark}). From Eq. 6 we get:

$$\Delta p = \frac{1}{q(\mu_n + \mu_p)} * \left(\frac{1}{\rho(\Delta p)} - \frac{1}{\rho_{dark}}\right) \qquad \text{Eq. 11}$$

Figure 18 represents experimental and simulated values of c-Si resistivity and $\rho_C(e^-)$, as a function of Δp as calculated from Eq. 11.

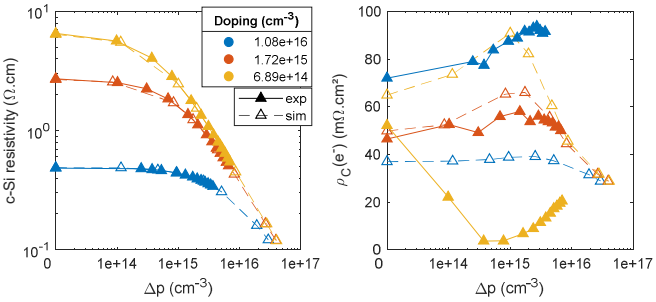

Figure 18: Experimental and simulated data of c-Si resistivity and $\rho_C(e^-)$ as a function of minority carrier density for rear illumination, for different wafer doping levels. The values at the y-intercept are the values in the dark.

First, we observe a very good agreement between simulation and experimental data for the c-Si resistivity values. Dark values are different and related to the doping density, and decrease with the increase in Δp, and even more as the doping level is low. Values for high Δp seem to regroup whatever the doping level is, indicating that a very high injection level is reached: for an illumination intensity of 10 Suns, $n = N_D + \Delta p$ is very close to $4 * 10^{16} cm^{-3}$ for each studied doping level, overriding so the initial carrier density.

As for $\rho_C(e^-)$, the agreement between experimental and simulated values is poor, especially for the least doped sample. First, we observe that in darkness experiment and simulation give different trends as a function of the doping level: simulation predicts a monotonous decrease with N_D, while no obvious trend is experimentally observed. Under illumination, simulation results show firstly an increase of ρ_C at low Δp values and then a decrease for higher values, for all doping densities. All ρ_C values tend toward a unique value at high Δp whatever the doping level is. However, experimentally, we got very different behaviors for all curves: the highest doped sample exhibited an increase of ρ_C almost until the end of the investigated Δp range, the medium doped sample showed a bell-shaped curve, and the least doped sample displayed a completely reverse behavior than simulated. The latter result should be taken with caution, as R^2 values for the TLM curves of the experimental data under illumination as low as 0.95 are obtained. Some strong defectivity is also confirmed with PL measurements on all samples. Despite great efforts to preserve the passivation of the samples, the experimental measurements are still greatly affected by defectivity, and therefore to the previously discussed biases, which are responsible for the large observed discrepancies.

Values representative of $\Delta p_{MPP} \sim 10^{15} cm^{-3}$ are obtained around 0.1 Sun for the least doped sample and 0.22Suns for the most doped sample. This suggests that we expect a relatively low difference on the value of $\rho_C(e^-)$ in the dark and at MPP conditions, except possibly for lowly doped samples.

Interestingly, we showed previously (Figure 16) that at high illumination, the homogeneity in Δp is better than at lower illuminations, so that the simulation results for $\rho_C(e^-)$ are expected to be more accurate at high illumination. This suggests that the non-monotonous behavior observed at intermediate illuminations may be an artifact of the TLM analysis under illumination. A particular attention should be paid to sample preparation and measurement procedure to ensure very good minority carrier density uniformity.

For the least doped samples, Δp is more homogeneous as the diffusion length is higher than in the other samples, however $n = \Delta p + N_D$ is less homogeneous in the range of studied illuminations, because $\Delta p \gg N_D$ so that doping does not even out n across the sample. As suggested in [35], N_D and Δp could have a similar effect on ρ_C. Even though this is unclear from our data, the fact that the amplitude of the variation of $\rho_C = f(\Delta p)$ is higher for the least doped sample both experimentally and by simulation could be explained this way.

However, the physics of the contact may be more complex than in our simulation approach, possibly explaining why we did not get the same trend in the dark of $\rho_C(e^-)$ versus c-Si doping, either experimentally or by simulation, and why we obtained an increase in $\rho_C(e^-)$ at low illuminations (if this is not due only to bias in the TLM analysis).

Also, intermediate illuminations, representative of the MPP conditions, are the most biased values and should be taken with caution. But our simulations suggest a moderate difference (below 30%) between the values determined in the dark and at $\Delta p = 10^{15} cm^{-3}$. This difference decreases as the c-Si resistivity decreases.

5. Conclusions

Evaluation and understanding of interface properties in passivated contact devices such as silicon heterojunction solar cells is of high importance for further contact engineering. TLM is a possible approach for such evaluation, as it enables contact resistance determination, and may be applied under illumination to account for device typical operating conditions. For this purpose, we presented and discussed a methodology for TLM sample preparation that is highly representative of a final SHJ cell, with similar design, thermal budget and passivation properties (prior to metallization), from which one can extract bulk resistivity and electron or hole contacts.

Experimental bulk silicon resistivity values were determined for various c-Si bulk parameters (doping, type) and illumination intensities using up-to-date models. We found a good agreement validating the TLM approach under illumination. The electron contact resistivity values extracted for these samples are also affected by illumination intensity.

TCAD 2D modelling was then used to account for different excitation conditions (frontside or backside illuminations), and compared to experimental results. It enabled to highlight a large influence of minority carrier spatial inhomogeneities on contact resistance results versus excess minority carrier density, underlining the difficulty of the approach. Results are likely to be more reliable in the dark and at very high injection level, where the inhomogeneities are lower than for intermediate injection levels.

More work is needed on this topic to identify how reliable measurement could be carried out. For instance, introducing intentional defectivity in the samples and in the simulations could be a way to assess more precisely their impact on the measurements. Different methods for ρ_C extraction under illumination could also be devised in future work to compare with the TLM approach, such as adaptations of the Cox and Strack's method [36], or numerical methods relying on the difference in Fermi level across the contact in 1D TCAD simulation.

The impact of the excess minority carrier density on the hole contact should also be addressed in more details, notably using high effective lifetime samples, in a rear illumination setup. Such an approach could also be pertinent for other types of contacts, such as tunnel oxides and poly-silicon contacts, and should be investigated.

6. Acknowledgment

This work was done in the framework of a PhD funded by the CEA. The authors thank Dr. Renaud Varache for valuable help for the simulations. The authors would also like to thank SunChemical for providing the hot-melt inks for patterning applications.

7. References

[1] K. Yoshikawa, W. Yoshida, T. Irie, H. Kawasaki, K. Konishi, H. Ishibashi, T. Asatani, D. Adachi, M. Kanematsu, H. Uzu, K. Yamamoto, Exceeding conversion efficiency of 26% by heterojunction interdigitated back contact solar cell with thin film Si technology, Sol. Energy Mater. Sol. Cells. 173 (2017) 37–42. https://doi.org/10.1016/j.solmat.2017.06.024.

[2] D. Adachi, J.L. Hernández, K. Yamamoto, Impact of carrier recombination on fill factor for large area heterojunction crystalline silicon solar cell with 25.1% efficiency, Appl. Phys. Lett. 107 (2015) 233506. https://doi.org/10.1063/1.4937224.

[3] W. Favre, D. Munoz, C. Roux, First European 25% Efficient Large Area Silicon Solar Cell: Path for European Premium PV Manufacturing is Open, (n.d.).

[4] X. Ru, M. Qu, J. Wang, T. Ruan, M. Yang, F. Peng, W. Long, K. Zheng, H. Yan, X. Xu, 25.11% efficiency silicon heterojunction solar cell with low deposition rate intrinsic amorphous silicon buffer layers, Sol. Energy Mater. Sol. Cells. 215 (2020). https://doi.org/10.1016/j.solmat.2020.110643.

[5] Z.C. Holman, A. Descoeudres, L. Barraud, F.Z. Fernandez, J.P. Seif, S. De Wolf, C. Ballif, Current Losses at the Front of Silicon Heterojunction Solar Cells, IEEE J. Photovolt. 2 (2012) 7–15. https://doi.org/10.1109/JPHOTOV.2011.2174967.

[6] D. Lachenal, D. Baetzner, W. Frammelsberger, B. Legradic, J. Meixenberger, P. Papet, B. Strahm, G. Wahli, Heterojunction and Passivated Contacts: A Simple Method to Extract Both n/tco and p/tco Contacts Resistivity, Energy Procedia. 92 (2016) 932–938. https://doi.org/10.1016/j.egypro.2016.07.104.
[7] L. Basset, W. Favre, D. Muñoz, J.-P. Vilcot, Series Resistance Breakdown of Silicon Heterojunction Solar Cells Produced on CEA-INES Pilot Line, 35th Eur. Photovolt. Sol. Energy Conf. Exhib. 721-724. (2018). https://doi.org/10.4229/35theupvsec20182018-2dv.3.21.
[8] R. Gogolin, M. Turcu, R. Ferre, J. Clemens, N.-P. Harder, R. Brendel, J. Schmidt, Analysis of Series Resistance Losses in a-Si:H/c-Si Heterojunction Solar Cells, IEEE J. Photovolt. 4 (2014) 1169–1176. https://doi.org/10.1109/JPHOTOV.2014.2328575.
[9] S.-Y. Lee, H. Choi, H. Li, K. Ji, S. Nam, J. Choi, S.-W. Ahn, H.-M. Lee, B. Park, Analysis of a-Si:H/TCO contact resistance for the Si heterojunction back-contact solar cell, Sol. Energy Mater. Sol. Cells. 120 (2014) 412–416. https://doi.org/10.1016/j.solmat.2013.06.026.
[10] H. Berger, Contact resistance on diffused resistors, in: Solid-State Circuits Conf. Dig. Tech. Pap. 1969 IEEE Int., IEEE, 1969: pp. 160–161.
[11] J. Schube, L. Tutsch, T. Fellmeth, M. Bivour, F. Feldmann, T. Hatt, F. Maier, R. Keding, F. Clement, S.W. Glunz, Low-Resistivity Screen-Printed Contacts on Indium Tin Oxide Layers for Silicon Solar Cells With Passivating Contacts, IEEE J. Photovolt. 8 (2018) 1208–1214. https://doi.org/10.1109/JPHOTOV.2018.2859768.
[12] J. Haschke, G. Christmann, C. Messmer, M. Bivour, M. Boccard, C. Ballif, Lateral transport in silicon solar cells, J. Appl. Phys. 127 (2020) 114501. https://doi.org/10.1063/1.5139416.
[13] H.H. Berger, Contact resistance and contact resistivity, J. Electrochem. Soc. 119 (1972) 507–514.
[14] M. Leilaeioun, W. Weigand, M. Boccard, Z.J. Yu, K. Fisher, Z.C. Holman, Contact Resistivity of the p-Type Amorphous Silicon Hole Contact in Silicon Heterojunction Solar Cells, IEEE J. Photovolt. (2019) 1–9. https://doi.org/10.1109/JPHOTOV.2019.2949430.
[15] S. Guo, G. Gregory, A.M. Gabor, W.V. Schoenfeld, K.O. Davis, Detailed investigation of TLM contact resistance measurements on crystalline silicon solar cells, Sol. Energy. 151 (2017) 163–172. https://doi.org/10.1016/j.solener.2017.05.015.
[16] S. Eidelloth, R. Brendel, Analytical Theory for Extracting Specific Contact Resistances of Thick Samples From the Transmission Line Method, IEEE Electron Device Lett. 35 (2014) 9–11. https://doi.org/10.1109/LED.2013.2290602.
[17] A. Danel, R. Varache, S. harrison, M. Vandenbossche, N. Rey, P. Leffilsatre, J. Gaume, A. Bettinelli, C. Roux, Versatile pilot line to support the heterojunction solar cell industrial development: busbar and busbar-less configurations, (2017).
[18] J.-H. Lan, J. Kanicki, A. Catalano, J. Keane, W. Den Boer, T. Gu, Patterning of transparent conducting oxide thin films by wet etching for a-Si: H TFT-LCDs, J. Electron. Mater. 25 (1996) 1806–1817.
[19] I. Haller, Y.H. Lee, J.J. Nocera Jr, M.A. Jaso, Selective wet and dry etching of hydrogenated amorphous silicon and related materials, J. Electrochem. Soc. 135 (1988) 2042.
[20] D.B.M. Klaassen, A unified mobility model for device simulation - I. Model equations and concentration dependence, Solid-State Electron. 35 (1992) 953–959.
[21] D.B.M. Klaassen, A unified mobility model for device simulation -II. temperature dependence of carrier mobility and lifetime, Solid-State Electron. 35 (1992) 961–967.
[22] W. Shockley, W.T. Read Jr, Statistics of the recombinations of holes and electrons, Phys. Rev. 87 (1952) 835.
[23] A. Richter, S.W. Glunz, F. Werner, J. Schmidt, A. Cuevas, Improved quantitative description of Auger recombination in crystalline silicon, Phys. Rev. B. 86 (2012). https://doi.org/10.1103/PhysRevB.86.165202.
[24] B.A. Veith-Wolf, S. Schäfer, R. Brendel, J. Schmidt, Reassessment of intrinsic lifetime limit in n-type crystalline silicon and implication on maximum solar cell efficiency, Sol. Energy Mater. Sol. Cells. 186 (2018) 194–199. https://doi.org/10.1016/j.solmat.2018.06.029.
[25] M. Garín, U. Rau, W. Brendle, I. Martín, R. Alcubilla, Characterization of a-Si:H/c-Si interfaces by effective-lifetime measurements, J. Appl. Phys. 98 (2005) 093711. https://doi.org/10.1063/1.2128047.
[26] L.-L. Senaud, Illuminated Contact Resistance Measurements to Investigate the Properties of Contact Stacks in Silicon Heterojunction Solar Cells, oral presentation at the 37th European Photovoltaic Solar Energy Conference and Exhibition (2020)
[27] P. Zhang, Y.Y. Lau, An exact field solution of contact resistance and comparison with the transmission line model, Appl. Phys. Lett. 104 (2014) 204102. https://doi.org/10.1063/1.4878841.
[28] V. Giglia, J. Veirman, R. Varache, E. Fourmond, Understanding of the Influence of the Surface Defectivity on Silicon Heterojunction Cell Performance, in: Underst. Influ. Surf. Defectivity Silicon Heterojunction Cell Perform., 2019: pp. 558–563. https://doi.org/10.4229/EUPVSEC20192019-2DV.1.59.
[29] M.J. Powell, S.C. Deane, Improved defect-pool model for charged defects in amorphous silicon, Phys. Rev. B. 48 (1993) 10815.
[30] R. Varache, J.P. Kleider, W. Favre, L. Korte, Band bending and determination of band offsets in amorphous/crystalline silicon heterostructures from planar conductance measurements, J. Appl. Phys. 112 (2012) 123717. https://doi.org/10.1063/1.4769736.
[31] K. Yang, J.R. East, G.I. Haddad, Numerical modeling of abrupt heterojunctions using a thermionic-field emission boundary condition, Solid-State Electron. 36 (1993) 321–330.
[32] H. Nagel, C. Berge, A.G. Aberle, Generalized analysis of quasi-steady-state and quasi-transient measurements of carrier lifetimes in semiconductors, J. Appl. Phys. 86 (1999) 6218–6221. https://doi.org/10.1063/1.371633.
[33] O. Nos, W. Favre, F. Jay, F. Ozanne, A. Valla, J. Alvarez, D. Muñoz, P.J. Ribeyron, Quality control method based on photoluminescence imaging for the performance prediction of c-Si/a-Si:H heterojunction solar cells in industrial production lines, Sol. Energy Mater. Sol. Cells. 144 (2016) 210–220. https://doi.org/10.1016/j.solmat.2015.09.009.
[34] V. Giglia, R. Varache, J. Veirman, E. Fourmond, Understanding of the influence of localized surface defectivity properties on the performances of silicon heterojunction cells, Prog. Photovolt. Res. Appl. 28 (2020) 1333–1344. https://doi.org/10.1002/pip.3330.
[35] D. Lachenal, P. Papet, B. Legradic, R. Kramer, T. Kössler, L. Andreetta, N. Holm, W. Frammelsberger, D.L. Baetzner, B. Strahm, L.L. Senaud, J.W. Schüttauf, A. Descoeudres, G. Christmann, S. Nicolay, M. Despeisse, B. Paviet-Salomon, C. Ballif, Optimization of tunnel-junction IBC solar cells based on a series resistance model, Sol. Energy Mater. Sol. Cells. 200 (2019) 110036. https://doi.org/10.1016/j.solmat.2019.110036.
[36] R.H. Cox, H. Strack, OHMIC CONTACTS FOR GaAs DEVICES, (n.d.) 8.